PASJ: Publ. Astron. Soc. Japan **58**, 931–943, 2006 December 25
© 2006. Astronomical Society of Japan.

Overdensity of X-Ray Sources in the Field of Two Nearby Clusters of Galaxies: XMM-Newton View of A 194 and A 1060

Murat HUDAVERDI, Hideyo KUNIEDA, Takeshi TANAKA and Yoshito HABA
Department of Physics, Nagoya University, Furo-cho, Chikusa-ku, Nagoya 464-8602
hudaverd@u.phys.nagoya-u.ac.jp
Akihiro FURUZAWA and Yuzuru TAWARA
EcoTopia Science Institute, Nagoya University, Furo-cho, Chikusa-ku, Nagoya 464-8602
and
E. Nihal ERCAN
Boğaziçi University, Physics Department, 80815 Bebek, Istanbul, Turkey

(Received 2006 May 16; accepted 2006 September 7)

Abstract

Two nearby clusters of galaxies, A 194 ($z = 0.018$) and A 1060 ($z = 0.0114$), have been analyzed for their X-ray point-source properties with XMM-Newton EPIC-PN data. A multi-band source detection technique was applied to both of the clusters, resulting in 46 sources from the A 194 field and 32 sources from the A 1060 field, respectively. The cumulative $\log(N)$–$\log(S)$ for a flux limit of $F_X \geq 1 \times 10^{-14}\,\mathrm{erg\,cm^{-2}\,s^{-1}}$ was calculated and compared with that of the Lockman Hole. A $\sim 3\sigma$ excess of X-ray sources was found for the cluster regions. Considering the higher fraction observed in optical studies from the clusters, we estimate that the cluster source density is 6-times higher than the blank-field source density, and 15-times higher than the local group. Our X-ray selected sources have luminosity values of $10^{39.6} \leq L_X \leq 10^{41.4}\,\mathrm{erg\,s^{-1}}$, in which X-ray emission from LMXBs, hot halos and starburst galaxies becomes noticeable. The significance of the source-density excess gradually vanishes for sources with $L_X \geq 10^{40.5}\,\mathrm{erg\,s^{-1}}$, at which point the source density becomes comparable to that of the blank-field level. Considering this confined low-luminosity range and the X-ray to optical luminosity ratios (L_X/L_B), the observed overdensity is ascribed to AGN fueling by its infall into cluster environment for $L_X \leq 10^{40.5}\,\mathrm{erg\,s^{-1}}$ in the X-ray luminosity function. However, the quenching of AGN activity by the deep cluster potential explains why the excess of the source density vanishes for brighter sources.

Key words: galaxies: clusters: individual (Abell 194, Abell 1060)

1. Introduction

X-ray studies of point sources within clusters are somewhat difficult, because observations of the galaxies are normally impeded by luminous diffuse emission of the Intra-Cluster Medium (ICM) and limited angular resolution of the telescopes. Recently, equipped with unprecedented spatial resolution and positional precision instruments, XMM-Newton and Chandra are uncovering higher fractions of galaxies in cluster fields compared to non-cluster fields.

Optical surveys suggest that AGNs are relatively rare in clusters compared to the field (Osterbrock 1960). Another survey by Gisler (1978) also found similar result based on a statistically improved sample. Dressler et al. (1985, 1999) report a fraction of $\sim 1\%$ AGN in the cluster environment, less than in the field (5%). However, they also mention the possibility of a higher AGN fraction in nearby clusters.

Several high-redshift clusters of galaxies have been reported to have an overdensity of X-ray point sources on their outskirts, which is naturally attributed to the infall-related fueling of active nuclei. Cappi et al. (2001) found 53 and 44 point sources from 3C 295 and RX J0030 fields, respectively, and reported an overdensity in these high redshifts ($z \sim 0.5$). Similarly, Molnar et al. (2002) detected significantly more sources around the rich cluster Abell 1995 ($z = 0.32$) than the fields. They also surveyed MS 0451 ($z = 0.55$), but found no evidence of an excess, so concluded that different classes of objects seem to dominate in different clusters. MS 1054−0321 ($z = 0.83$) was reported to have 47 X-ray sources by Johnson et al. (2003) and found to have a $\sim 2\sigma$ excess compared to the non-cluster fields. Cappelluti et al. (2005) conducted a systematic analysis of the X-ray source population around 10 distant clusters ($0.24 \leq z \leq 1.2$). They found excess values relative to the non-cluster fields of more than a factor of 2σ per field. Ruderman and Ebeling (2005) analyzed Chandra data of 51 clusters with the redshift range $0.3 \leq z \leq 0.7$, and detected an 8σ significant excess in the point-source density within 3.5 Mpc of the cluster centers.

At low redshifts, the excess seems to be largely due to low-luminosity AGN associated with the cluster. One early study by Henry and Briel (1991) with ROSAT for A 2256 ($z = 0.06$) found twice as many sources as expected from blank fields. Lazzati et al. (1998), using the wavelet analysis technique on ROSAT PSPC observations of nearby clusters, A 1367 ($z = 0.022$) and A 194 ($z = 0.018$), detected 28 and 26 sources in the respective fields. A 1367 was also eventually observed by Chandra, and 59 sources were detected (Sun, Murray 2002). Finally, Martini et al. (2006) spectroscopically confirmed a large AGN population in low-redshift clusters ($0.05 \leq z \leq 0.31$).

In this paper, we report on X-ray point sources observed

Downloaded from https://academic.oup.com/pasj/article/58/6/931/1445864 by Yildiz Teknik University Library (YTU) user on 25 February 2022

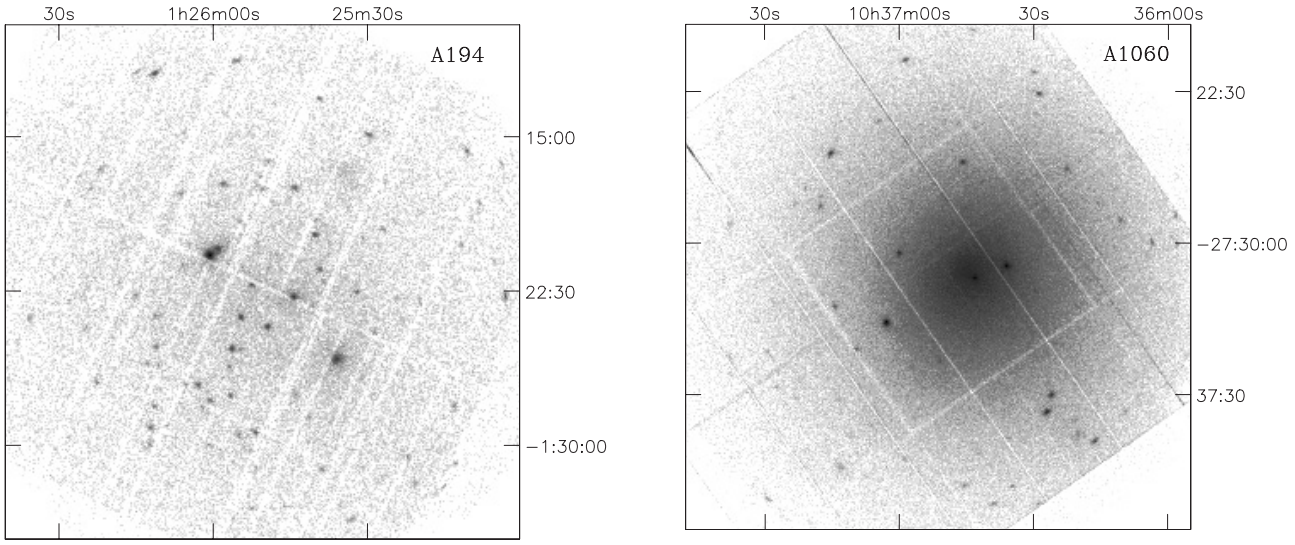


Fig. 1. Adaptively smoothed XMM-Newton EPIC images of A 194 (left) and A 1060 (right) clusters in the 0.3–10 keV band. Images have a size of $25' \times 25'$ and a pixel-size of $5''$. The smoothing and contrast are selected in order to highlight point sources. The images are adjusted with north up and east left.

in the field of two nearby clusters, A 194 ($z = 0.018$) and A 1060 ($z = 0.0114$). The emission from individual sources in these clusters stands out particularly well, since the diffuse emission is not very luminous. A 194 is selected as a very faint ($L_X \sim 10^{42}\,\mathrm{erg\,s^{-1}}$), poor cluster with no clear extended emission and no X-ray peak. The cluster is known as a linear cluster for its brightest member galaxies, which are aligned in the direction of northeast to southwest. The temperature distribution of ICM is uniform at $kT = 2.7$ keV. The cluster is also a strong radio emitter. Conversely, A 1060 is X-ray brighter ($L_X \sim 1 \times 10^{43}\,\mathrm{erg\,s^{-1}}$) than A 194. The cluster is dominated by a pair of giant ellipticals, NGC 3309 and NGC 3311. A circularly symmetric smooth surface brightness, isothermal ICM ($kT = 3.3$ keV) and being populated by at least six bright NGC galaxies in the central region make the source very suitable for our survey.

We adopt $H_0 = 75\,\mathrm{km\,s^{-1}\,Mpc^{-1}}$ and a cosmological deceleration parameter of $q_0 = 0.5$. The luminosity distances to A 194 and A 1060 are 73 Mpc and 46 Mpc, and an angular size of 1 arcmin corresponds to 20.5 kpc and 13 kpc, respectively. The quoted uncertainties for the best-fit parameters of spectral fittings are given for the 90% confidence range.

2. Observations and data reduction

We used X-ray data obtained by XMM-Newton observations which covered a major portion of the cluster emission with a large collecting area. The three European Photon Imaging Camera (EPIC) instruments, the two EPIC-MOS detectors (Turner et al. 2001) and the EPIC-PN detector (Strüder et al. 2001), were used.

The A 194 cluster field was observed with the XMM-Newton satellite in revolution 557 on 2002 December. The cameras were operated in the Prime Full Window mode with thin filters. A 1060 was observed in 2004 June in revolution 834. A medium filter was used for three EPIC cameras. In our study, the Lockman Hole was chosen and referred to as a blank field to compare with the cluster fields. We selected four recent long late observations of the Lockman Hole. The total exposure was ~ 400 ks. All three cameras in the four observations were operated with the medium filter. The difference in the count rates from using medium and thin optical filters was negligible. It was less than 2% at $E > 0.5$ keV, and obtained the highest value of $\sim 10\%$ at 0.3 keV. A summary of the observations is given in table 1.

The event lists were generated from the Observation Data Files (ODF) by the tasks EMCHAIN and EPCHAIN. We then selected the events with PATTERN 0–12 for MOS and single & double pixel events (PATTERN 0–4) for PN. In order to clean the contamination by soft proton flares, the extracted light curves for MOS (10–12 keV) and PN (12–14 keV) were clipped above and below $2.7\,\sigma$ of the average count rate. Finally, the resulting Good Time Intervals (GTI) selections were applied to the event lists to produce filtered event files.

3. Source Detection

We performed multi-band source detection on the EPIC images in the soft band of 0.3–1 keV (S), medium band 1–1.6 keV (M), and hard band 1.6–10 keV (H). The main concern with this energy selection is to identify the diversity of sources with relative sensitivities at different energy bands. Principally, the diagnosis of intrinsic absorption effects and power-law emission is intended. This energy selection also splits the counts evenly, which is statistically more favorable.

Source detection is performed with two different SAS tasks in order to carry out comparable detection. These are the maximum-likelihood (Cash 1979) method "EMLDETECT" and the wavelet-detection routine "EWAVELET" (Damiani et al. 1997). The three X-ray images were scanned by using both methods. The relation between the likelihood limit (L) and the Gaussian probability (P) is given as $L = -\ln P$.

Downloaded from https://academic.oup.com/pasj/article/58/6/931/1445864 by Yildiz Teknik University Library (YTU) user on 25 February 2022

Table 1. Log of observations.

Source	OBS-ID*	Date	Live time (ks)			Filter
			MOS1	MOS2	PN	EPIC
A 194	0136340101	2002.12.23	18.6	19.1	20.6	thin
A 1060	0206230101	2004.06.29	37.7	38.4	57.2	med.
LH†	0147510901	2002.10.19	48.6	50.8	52.8	med.
	0147511601	2002.11.27	105.1	106.6	97.2	med.
	0147511701	2002.12.04	92.7	93.4	86.2	med.
	0147511801	2002.12.06	77.5	78.7	63.9	med.

* Observation id. † Lockman Hole.

We selected a minimum likehood of $ML = 10$ and a 4σ Gaussian of the signal-to-noise ratio, at which a probability of $\sim P = 3.2 \times 10^{-5}$ was attained by both values. These methods take into account vignetting and PSF variations by means of relative exposure maps. The obtained lists were compared, and sources falling outside of a 25 arcmin circle were removed. The final list was prepared by merging the three energy-band source lists for both PN and MOS into a summary source list with the SAS command "SRCMATCH".

With the source detection routines mentioned above, the final merged lists contain 56 and 32 point sources for A 194 and A 1060, respectively. The Lockman Hole observations have longer exposures and no contamination by extended X-ray emission, as opposed to those of the cluster fields; thus, the number of detected sources (173) is naturally higher. The sources are expected to have different spectral types, and hence not all sources are detected significantly in all three energy bands. It is also worth noting that some of the sources have been detected by only MOS or PN. These sources are located either in or around chip gaps. The source numbers for each camera and each energy band are given in table 2. The minimum flux values at 2–10 keV among the detected sources are 1.28×10^{-15} erg cm^{-2} s^{-1} and 1.23×10^{-15} erg cm^{-2} s^{-1} for A 194 and A 1060. We use only PN data for the rest of the analysis, because it has higher sensitivity than MOS cameras.

Table 2. Number of the detected sources for each camera and energy band.

Source	Total number*		Source numbers			
			S‡	M§	H‖	Total#
A 194	56	MOS	30	22	38	46
		PN	37	25	26	46
A 1060	32	MOS	20	17	17	27
		PN	27	21	20	32
LH†	173	MOS	79	78	81	123
		PN	98	81	54	123

* Total number of sources for the final merged list.
† Lockman Hole.
‡ Soft, 0.3–1 keV.
§ Medium, 1–1.6 keV.
‖ Hard, 1.6–10 keV.
Total number of sources detected by each camera.

4. X-Ray Color Diagrams

We have developed a color–diagram to determine the average spectral properties of a given sample, because not all of the sources have statistically sufficient photon counts to allow individual spectral fitting. The color diagram is known to be a sensitive tool to define source types (White, Marshall 1984). We defined two hardness ratio (HR) values: and plot soft ratio HR1 = (M − S)/(M + S) against hard ratio HR2 = (H − M)/(H + M). The hardness ratios were calculated from the net count rates in the soft, medium and hard bands obtained by the source detection routines. The net counts of the three energy bands and the hardness ratios for the detected sources are listed in the appendix (table 6 and 7).

4.1. Simulations

We conducted simulations for each cluster to predict the locations of various sources in the color–diagram. The simulations of both clusters are practically equivalent. Therefore, we show only the grids from the A 194 simulations in figure 2. In all simulations, the hydrogen column densities were fixed at the galactic absorption values: 3.8×10^{20} cm^{-2}, 4.9×10^{20} cm^{-2} and 5.7×10^{19} cm^{-2} for A 194, A 1060 and the Lockman Hole, respectively. We used a fixed metal abundance of 0.3 of solar in our simulations, which is the average galactic value. The black grid shows the variation of the power-law model with intrinsic absorption (zpha∗pow of XSPEC). As X-ray colors of the sources move to the left (HR2 decreases) on the grid, the photon index, Γ, increases from 1.0 to 3.0 in 0.1 steps. The increasing absorption ($N_{\rm H}$ = 0.01, 0.05, 0.10, 0.50, 1.00, and 3.00×10^{22} cm^{-2}) pushes the sources toward the upper right. In other words, as the absorption increases, both the HR1 and HR2 values increase. We also simulated a multi-component model of MEKAL (Mewe et al. 1985) and the absorbed power law for those galaxies with thermal plasma emission. The power-law parameters were retained at the same values, whereas a temperature value of 0.5 keV was used. This value is sufficient to represent the sub-keV levels of thermal emission, as produced by hot gas of normal galaxies. The black grid of a simple power-law model is entirely inclined down with the additional thermal model. This curved grid is colored in gray (figure 2) and displays the expected location of multi-component sources in the color–diagram.

Downloaded from https://academic.oup.com/pasj/article/58/6/931/1445864 by Yildiz Teknik University Library (YTU) user on 25 February 2022

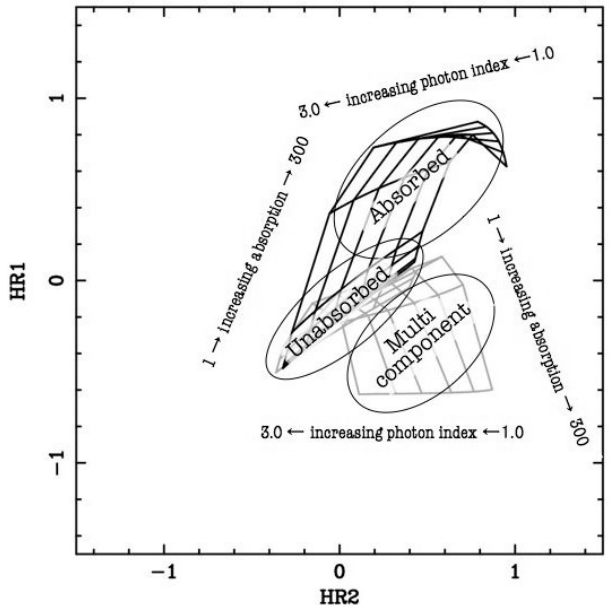


Fig. 2. Simulations of zpha∗(pow) (black) and MEKAL+ zpha∗(pow) (gray) shown in grids. X-ray colors of sources with power-law spectra with photon index Γ gets the values from 1.0 to 3.0 in 0.1 steps as the grid moves left. Increasing absorption ($N_{\rm H}$ = 0.01, 0.05, 0.10, 0.50, 1.00, and $3.00 \times 10^{22}\,{\rm cm}^{-2}$) effects push sources toward the upper right in the diagram.

5. Classification of Sources

In this section, we explain the type of sources based on the definitions from the diagram. A uniform classification criteria is defined for the two clusters. Table 3 shows our classification of sources based on the HR values of the X-ray color–diagrams. The classification scheme is roughly sketched with the ellipses on the grids of figure 2. We acknowledge that the color–diagram is admittedly basic, but it can be regarded as being a reasonable method to infer appreciable knowledge on the physical nature of faint sources.

Table 3. X-ray color classifications. The sources with only-soft or only-hard band detectable emission are classified as indeterminate sources and do not appear in this table. Their hardness ratio values are, as they get the name after, *indeterminate.*

Classification	Definition
Unabsorbed	$-0.6 \leq$ HR1 ≤ 0.0, $-0.4 \leq$ HR2 ≤ 0.5
Absorbed	$0.0 \leq$ HR1 ≤ 0.8; $(-1, 1)^{*}$
Multi component	HR1 ≤ -0.4, $0.3 \leq$ HR2
Super Soft	HR2 $= -1.0^{\dagger}$
Super Hard	HR1 $= 1.0^{\ddagger}$; $(1, -1)^{\S}$

* Sources with no detectable medium-band emission.
† Sources with no hard-band emission.
‡ Sources with no soft-band emission.
§ Sources with only medium-band emission.

5.1. *Unabsorbed Sources*

Most of the sources, which were detected in all three-bands, were fitted with a single power-law model. The photon indexes are in the physically tolerable range ($0.8 \leq \Gamma \leq 2.5$), with the majority of sources clustering at around the $\Gamma = 1.7$ value. The sources with a hardness ratio value of $-0.6 \leq$ HR1 ≤ 0.0, $-0.4 \leq$ HR2 ≤ 0.5 are defined as unabsorbed sources. We found 13 and 11 sources falling into this class for A 194 and A 1060, respectively. Source #4 from the A 1060 field is a good example of this kind. Figure 4A shows a single power-law model with a photon index of $\Gamma = 2.03^{+0.27}_{-0.24}$. The source has 750 counts in the total band 0.3–10 keV and the luminosity is $L_{\rm X} = 10^{40.2}\,{\rm erg\,s^{-1}}$ in the 2–10 keV band.

5.2. *Absorbed Sources*

The simulations showed (subsection 4.1) that increasing absorption pushes the sources toward the upper right in the diagram. In figure 3 we highlight the sources with the soft range $0.0 \leq$ HR1 ≤ 0.8 by star signs in the diagrams. These are defined as the absorbed sources. The sources were well fitted with the absorbed power-law model. The intrinsic absorptions

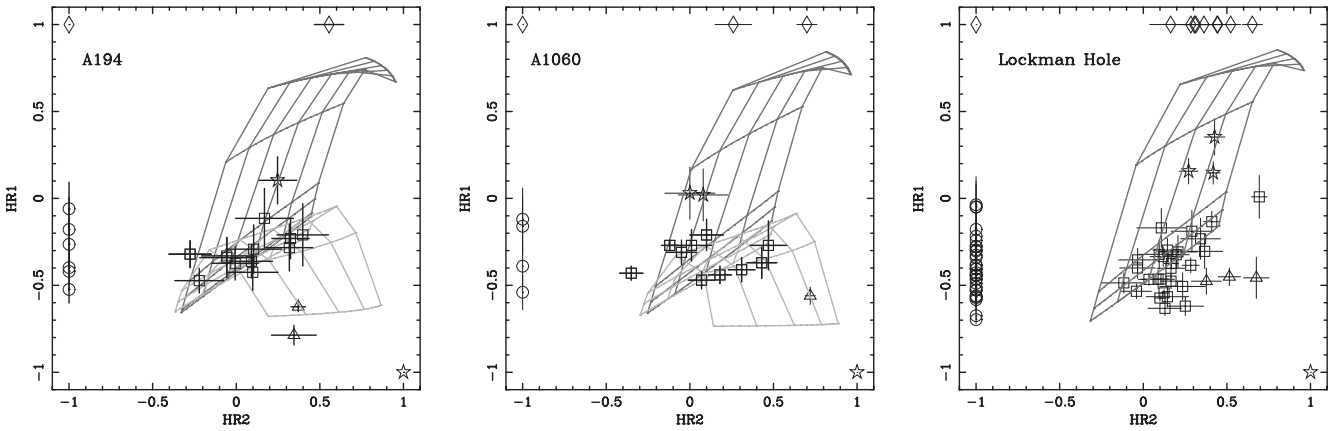


Fig. 3. X-ray color–diagrams of A 194, A 1060 and Lockman Hole showing the source classification defined in table 3. Each symbol represents a different type of source; squares (□) are un-absorbed, stars (⋆) are absorbed, triangles (△) are multi-component sources, diamonds (◇) are hard sources and circles (○) are soft sources. The grids show the simulated models (see subsection 4.1 for details).

Downloaded from https://academic.oup.com/pasj/article/58/6/931/1445864 by Yildiz Teknik University Library (YTU) user on 25 February 2022

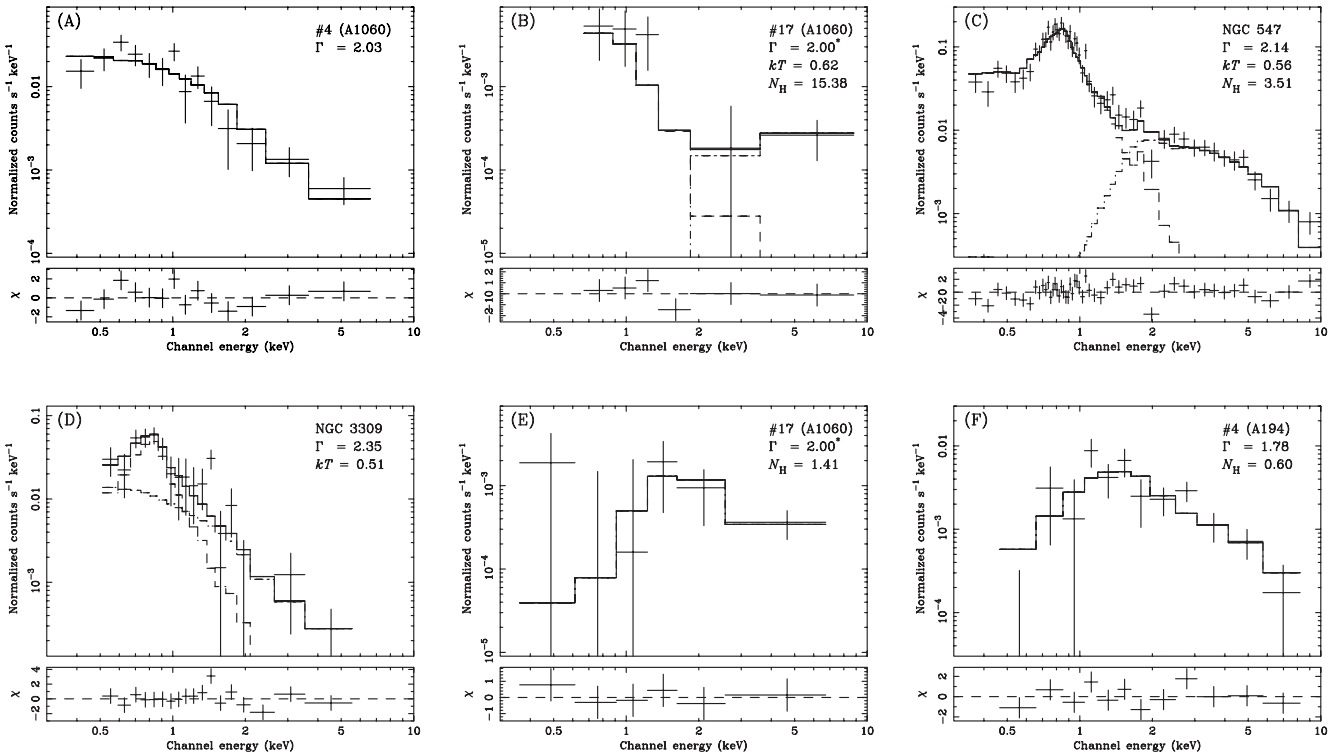


Fig. 4. EPIC-PN spectra with best-fit models. A, source #4 (A 1060); B, source #17 (A 1060); C, source #1—NGC 547 (A 194); D, source #5—NGC 3309 (A 1060); E, source #14 (A 1060); F, source #4 (A 194).

values are $N_{\rm H} \geq 0.5 \times 10^{22}\,{\rm cm}^{-2}$. Source #17 from A 1060 is one of the brightest sources in this classification. About 60% of the emission is detected below 1 keV and the remaining 40% is from above 1.6 keV, with no detectable emission from the 1–1.6 keV medium band. Figure 4B shows the X-ray spectrum of the source. The best-fit parameters are $N_{\rm H} = 15.38 \times 10^{22}\,{\rm cm}^{-2}$, $\Gamma = 2.00$ (fixed) and a thermal component of $kT = 0.62^{+0.97}_{-0.39}$ keV. The rest-frame luminosity is $L_{\rm X} = 10^{39.5}\,{\rm erg\,s}^{-1}$ for PN (120 counts in 0.3–10 keV band). Absorbed sources with no detectable medium-band emissions are seen at the HR1, HR2 = $(-1, 1)$ point on the color–diagrams. Four sources from A 194 and 6 sources from A 1060 are classified in this group (table 4).

Table 4. Number of sources in each group.

Type	A 194	A 1060	Lockman Hole
Unabsorbed	13	11	28
Absorbed	4	6	4
Multi component	2	1	3
Super soft	5	4	32
Super hard	3	4	15
Indeterminate soft	12	6	31
Indeterminate hard	6	1	10
Total	46	32	123

5.3. Multi Component Sources

The spectra of some sources were not acceptably fitted with a single power law, and the presence of a soft excess was evident. The fit was significantly improved by adding a thermal-plasma model to the main power-law continuum. The thermal-model was parameterized by the MEKAL plasma model (Mewe et al. 1985). The hardness ratio values between HR1 ≤ -0.4 and HR2 ≥ 0.3 correspond to multi-component sources. We detected 3 sources in the cluster fields, 2 of which are in the A 194, and 1 in the A 1060 field. The spectra of source #1—NGC 547 (figure 4C) from A 194 and #5—NGC 3309 (figure 4D) from A 1060 display the characteristics of this group. NGC 547 is classified as a type-2 AGN at $z = 0.01823$. The best-fit parameters are $kT = 0.56 \pm 0.03$ keV, $\Gamma = 2.14^{+0.82}_{-0.73}$ and $N_{\rm H} = 3.51^{+2.62}_{-1.98} \times 10^{22}\,{\rm cm}^{-2}$. The source has a rest-frame luminosity of $L_{\rm X} = 10^{42.1}\,{\rm erg\,s}^{-1}$ in the 2–10 keV band. The photon count is 1375 in the 0.3–10 keV band. NGC 3309 has a thermal gas with a temperature of $kT = 0.51^{+0.13}_{-0.18}$ keV, and a power-law index of $\Gamma = 2.35^{+0.42}_{-0.77}$. The source has a luminosity of $L_{\rm X} = 10^{39.8}\,{\rm erg\,s}^{-1}$ in the 2–10 keV band. The spectral best-fit temperature values of the multi-component sources are confined to $0.5 \leq kT \leq 1.0$ keV, which is the anticipated range for thermal emission from normal galaxies.

5.4. Super Soft and Hard Sources

We have detected 8 sources with no significant emission above 1.6 keV. These sources, which are located at HR1 = -1 in the color diagram, are defined as super-soft sources (SSS)

Downloaded from https://academic.oup.com/pasj/article/58/6/931/1445864 by Yildiz Teknik University Library (YTU) user on 25 February 2022

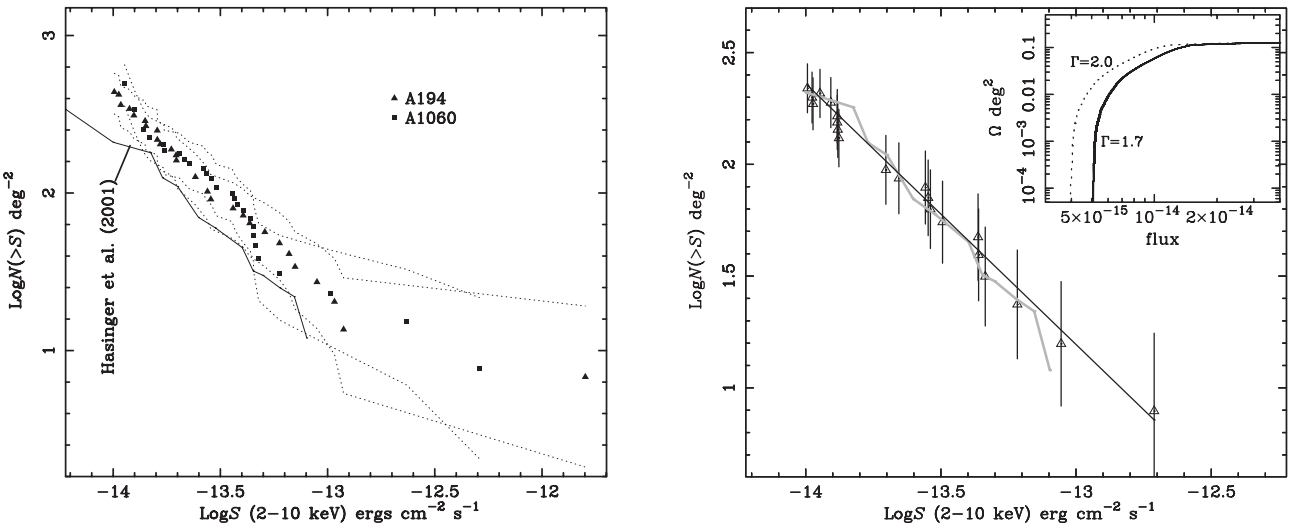


Fig. 5. Left panel: log(N)–log(S) of the identified sources of our samples A 194 (triangle—△) and A 1060 (box—□) is compared with the field of the Lockman Hole (Hasinger et al. 2001). The dotted lines show the statistical and calibration errors. Right panel: log(N)–log(S) for Lockman Hole is fitted with a power-law model $N\ (>S) = K \times S^{-\alpha}$. The best-fit values are $\alpha = 1.16^{+0.20}_{-0.25}$ and $K = 1.45 \times 10^{-14}\,\mathrm{deg}^{-2}$. The model and the Lockman Hole plot of Hasinger et al. (2001) are shown in black and gray lines, respectively. Error bars represent $1\,\sigma$ statistical constraints and 10% absolute calibration errors (Kirsch 2006). Survey area, $\Omega\,\mathrm{deg}^2$, is plotted against the sensitivity flux limit at the top corner. The solid and dashed lines correspond to the photon index values of $\Gamma = 1.7$ and $\Gamma = 2.0$ to convert the count rate to flux.

[except HR2, HR1 = (1, −1), see subsection 5.5]. The features of these sources are quite similar to those found in Large Magellanic Cloud and M 31 (e.g., Kahabka, van den Heuvel 1997; Pietsch et al. 2005). On the contrary, 7 sources have no detectable emission below 1.0 keV, which are consequently named as super hard sources (SHS). The diamond marks in the color–diagrams (figure 3) stand for SHS. As stated by the definitions, SHS have values of HR1 = 1.0, and they are found at the top of the diagrams. Sources #14 of A 1060 and #4 of A 194 exhibit the characteristic of SHS. The counts of these sources in the 0.3–10 keV band are 104 and 149, respectively. Figure 4E and F show spectral fits with a simple power law model. The photon indexes of sources #14 and #4 are $\Gamma = 2.00$ (fixed) and $\Gamma = 1.78^{+0.82}_{-0.65}$. The intrinsic absorption values appear to be marginal, but significant, relative to the galactic values. The best-fit values are $N_{\mathrm{H}} = 1.41^{+5.88}_{-1.08} \times 10^{22}\,\mathrm{cm}^{-2}$ and $N_{\mathrm{H}} = 0.60^{+0.83}_{-0.37} \times 10^{22}\,\mathrm{cm}^{-2}$, respectively. The rest-frame luminosities are $L_{\mathrm{X}} = 10^{40.1}\,\mathrm{erg\,s}^{-1}$ and $L_{\mathrm{X}} = 10^{40.7}\,\mathrm{erg\,s}^{-1}$ in the 2–10 keV band.

5.5. *Indeterminate Soft and Hard Sources*

A further classification of the sources is given for indeterminate sources. These sources have detectable emission only below 1 keV, or only above 1.6 keV, making their hardness ratio values undefined. Because they can not be classified by a criteria based on the color diagram, we name them indeterminate sources. The indeterminate source numbers in the cluster field are 18 for soft sources and 7 for hard, while 31 are for soft and 10 for hard sources in the Lockman Hole field. The majority of them are on the outskirts ($R \geq 5$ arcmin), and might be unrelated to the clusters. The nature of these sources may include several types, and are open to debate.

The number distribution of the sources for the classification mentioned above is given in table 4. The number of soft sources in the Lockman Hole is exceptionally high, about half of the sources. This is mainly due to the higher efficiency of the detector at lower energies and no extended ICM emission in the Lockman Hole field that would bury point-like emissions. In our study, the Lockman Hole is used as non-cluster control field to compare with the cluster regions; therefore, the classification given in table 4 is sufficient for our objectives. A further separation is beyond of the scope of our paper. The reader is referred to a review of Mainieri et al. (2002) for a detailed discussion of the physical nature of the sources found in the Lockman Hole, combining X-ray data with optical/near IR data.

6. log(N)–log(S)

The sum of inverse areas of all sources brighter than flux S, $N\ (>S)$, is defined as the cumulative number per square degree. Using the integrated formula of source numbers in units of deg^{-2},

$$N\ (>S) = \sum_{i=1}^{n} \frac{1}{\Omega_i}\ (\mathrm{deg}^{-2}), \tag{1}$$

where n is the detected source number and Ω_i is the sky coverage for the flux of the i-th source, the relation between number and flux is derived. Figure 5, left panel, shows a comparison of the obtained log(N)–log(S) plot for A 194 and A 1060 and that of the Lockman Hole measured by Hasinger et al. (2001). The dotted lines represent the sum of $1\,\sigma$ Poisson errors in the source counts and the systematic instrumental errors. The systematic instrumental errors related to vignetting

Downloaded from https://academic.oup.com/pasj/article/58/6/931/1445864 by Yildiz Teknik University Library (YTU) user on 25 February 2022

and the point-spread function (PSF) are considered to be 3.5% for an off-axis source by Saxton (2003). We use 10% as the absolute calibration error, which dominates the other sources of error (Kirsch, 2006). The limiting flux levels are 1.284×10^{-15} erg cm^{-2} s^{-1} (A 194) and 1.279×10^{-15} erg cm^{-2} s^{-1} (A 1060) in the 2–10 keV band. The characteristic of the solid angle is the same as that for the clusters and the field: the survey area decreases with the flux. In clusters, due to extended emission, faint sources can not be easily detected in the center, and thus they appear at the outskirts. However, in the field there is no extended emission to bury faint sources. Faint sources are detectable only at smaller off-axis angles where PSF and vignetting effects are smaller. We used a flux limit of 1×10^{-14} erg cm^{-2} s^{-1} in our survey to avoid this ambiguity. A significant ($\sim 3\sigma$) X-ray source excess is found from cluster fields relative to the Lockman Hole.

In figure 5 right panel we present our Lockman Hole source numbers at 2–10 keV, which are in excellent agreement with the result of Hasinger et al. (2001). The Lockman Hole log(N)–log(S) is described by a power-law model as a function of a dimensionless S as

$$N\ (>S) = 1.45 \times 10^{-14} \times S^{-1.16^{+0.20}_{-0.25}}, \quad (2)$$

with a slope of $\alpha = 1.16^{+0.20}_{-0.25}$ and a normalization of $K = 1.45 \times 10^{-14}$ deg^{-2}. The solid line shows the best-fit model (figure 5 right panel) compared with the result of Hasinger et al. (gray line). The survey area, Ω deg^2, as a function of the limiting fluxes in the 2–10 keV band can be seen in the same figure as well. The energy conversion factor (ECF) used to derive the flux from counting rate was calculated to be $0.51 \pm 0.09 \times 10^{-11}$ erg cm^{-2} s^{-1}, with the assumptions of $\Gamma = 1.7$ and the galactic value of the hydrogen column density. The ECF errors correspond to the photon index range of $\Gamma = 1.7 \pm 0.3$.

Log(N)–Log(S) conventionally shows source numbers per unit sky area. An optimum comparison of the clusters with the field would be the source number density per unit volume, as outlined by Finoguenov et al. (2004). Unfortunately, in our survey distance information is not accessible for all the sources. The photometric redshift value is available only for $\sim$ 10% of the X-ray detected sources. We used a subtraction method for an implicit approximation, assuming that the source density enhancement is attributable to the density contribution of galaxies in the cluster gravitational potential. This method deduces the Lockman Hole source density from that of the clusters by carefully dealing with the errors. It is a tricky job because of the statistical errors and cosmic variance, which is a field-to-field variation of the blank field. Based on the most sensitive measurement to date, the cosmic variance is reported to be less than 15% in the 2–10 keV band (Cappelluti et al. 2005). Figure 5 shows that our source density values correspond to 438 ± 87 sources deg^{-2} for A 194 and 494 ± 97 sources deg^{-2} for A 1060 around our flux limit of 1×10^{-14} erg cm^{-2} s^{-1}. At this flux level, a density of 220 ± 33 sources deg^{-2} from Lockman Hole was calculated (errors, 15% cosmic variance).

If we perform the calculations by using the minimum possible source-density values from clusters and the maximum source density level for the Lockman Hole, the number densities are 130 sources deg^{-2} for A 194 and 144 sources deg^{-2} for A 1060. This calculation for the worst-case scenario verifies that at least $\sim$ 30% of the detected X-ray sources are cluster members. Encouraged by this result, we estimated the unbinned X-ray Luminosity Function (XLF) per unit volume $\Phi(L_X)$ (Mpc^{-3}), as shown in figure 6. The function was calculated from the relation

$$\Phi(L) = \frac{N}{\int_{L_{\min}}^{L_{\max}} \int_{z_{\min}(L)}^{z_{\max}(L)} \Omega(L, z)(dV/dz)\, dz dL}, \quad (3)$$

where N is the number of objects with luminosities and redshifts in the interval of $\Delta L \Delta z$ and dV/dz is the volume element. The method is described in detail by Page and Carrera (2000) and Georgantopoulos et al. (2005). The plot covers a luminosity range of $39.5 \leq \log(L_X) \leq 42.1$ erg s^{-1}. There are a few luminosity levels with a negative slope in the plot. These luminosity levels are points where the source density of the clusters is comparable to that of the Lockman Hole.

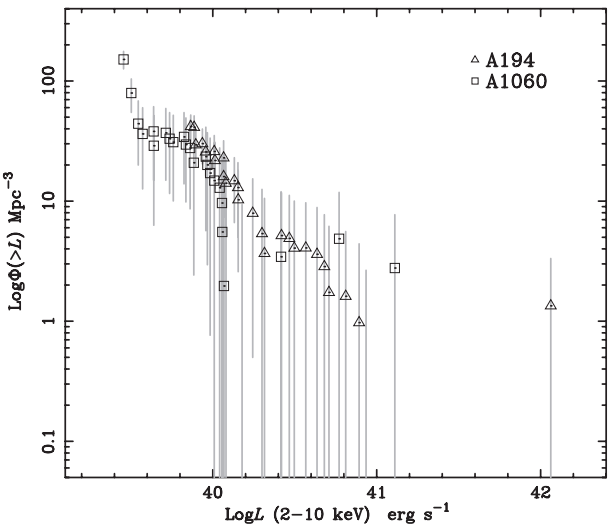


Fig. 6. Integrated source density Φ against L_X for A 194 (triangle—△) and A 1060 (box—□). There is a confusion around high luminosity levels since the number density of the sources at these luminosity levels is close to the density of the Lockman Hole (see section 6).

7. Discussion

We analyzed XMM-Newton observations of clusters of galaxies A 194 and A 1060. We derived and studied log(N)– log(S) (figure 5) and the unbinned XLF (figure 6). The cluster X-ray source fraction was estimated to be $\sim 3\sigma$ higher relative to the Lockman Hole at $F_X = 1 \times 10^{-14}$ erg s^{-1} flux limit. These clusters were studied previously at optical wavelengths. The galaxy luminosity function (GLF) is one of the basic statistics of the properties of galaxies. Oemler (1974) studied 15 clusters' GLF, including A 194, and reported that the clusters and the blank-field have similar shapes. Christlein and Zabludoff (2003) studied R-band GLFs of 6 nearby clusters, and A 1060 was the nearest cluster in their survey sample. Based on their study, a factor 75 higher galaxy density was estimated on average for the clusters with respect

Downloaded from https://academic.oup.com/pasj/article/58/6/931/1445864 by Yildiz Teknik University Library (YTU) user on 25 February 2022

to non-cluster fields. The highest fraction was measured at $M_R = -18.75$ with $\Phi(M_R)/dM_R = 0.07\,\mathrm{Mpc}^{-3}$ galaxies, which corresponds to a factor ~ 175 above the non-cluster field density. The luminosity range of our survey sample was $2.88 \times 10^{39}\,\mathrm{erg\,s^{-1}} \leq L_X \leq 1.15 \times 10^{42}\,\mathrm{erg\,s^{-1}}$. At such low-luminosity levels, the emission from Low Mass X-Ray Binaries (LMXBs), hot halo and low-luminous AGNs (LLAGN) should be taken into consideration. We investigated soft and hard emission by means of color–diagrams (figure 3), and found that the majority of sources have a hard spectral type. If these galaxies do not possess an AGN, the emission is expected to be produced by the unresolved population of LMXBs (Sarazin et al. 2001; Blanton et al. 2001). Three galaxies were detected with soft thermal emission from diffuse galactic gas. The temperature values were found to be ($0.2\,\mathrm{keV} \leq kT \leq 0.8\,\mathrm{keV}$) in the average range, depending the bulge size of the galaxy.

To address the origin of X-ray emission we checked (i) the X-ray to optical luminosity ratio (L_X/L_B) and (ii) the binned XLF by comparing with noncluster fields. Since the B-band magnitudes are sensitive to dust and recent star formation, the X-ray to optical luminosity ratio (L_X/L_B) provides important constraints on ISM: hot halo and LMXBs (Matsushita 2001; Sarazin et al. 2001; Irwin et al. 2002). Alternatively, if the sources without any optical counterparts are LLAGNs, we can compare our XLF to AGN source density of groups of galaxies (Elvis et al. 1984) and that of the blank-fields (Miyaji et al. 2000; Ueda et al. 2003).

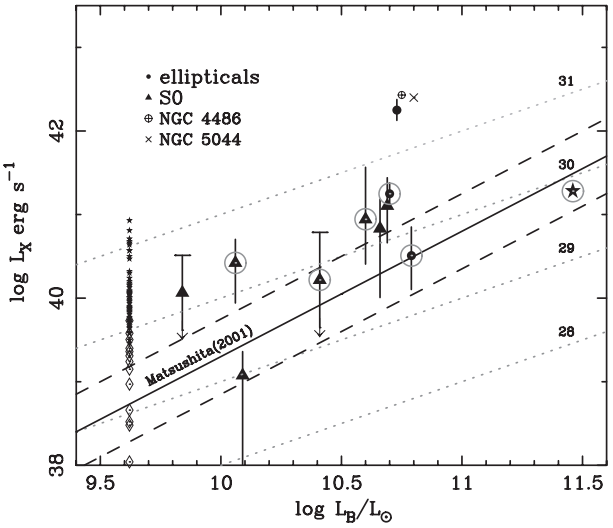


Fig. 7. L_X–L_B relation for bright elliptical and spiral galaxies. The L_X values were calculated within $< 4r_e$ of galaxies in the 0.3–10 keV band, where r_e is the effective radius for each galaxy. The symbols indicate galaxy classifications for cluster elliptical (filled circles), cluster spirals (filled triangles). The circled sources are those from A 1060 region. The crossed circle stands for NGC 4486 (Virgo cD) and the cross is the X-ray extended elliptical NGC 5044 from Matsushita (2001). The gray dashed lines shows the slopes for log (L_X/L_B) ratios of 28, 29, 30, and 31. The solid line is the distribution function for X-ray compact galaxies defined by Matsushita (2001) with 90% confidence limits (dashed lines).

7.1. X-Ray to Optical Luminosity Relation

The hard-band (2–10 keV) X-ray luminosity values are plotted against the optical blue luminosities in figure 7. The properties of 11 optically identified galaxies are given in table 5. The effective radius of each galaxy, r_e, the distance from galaxy center within which half of the optical luminosity is emitted, and the apparent blue magnitudes, m_B are taken from de Vaucouleurs et al. (1991, hereafter RC3). The absolute

Table 5. Optical properties of galaxies identified for A 1060 and A 194.

Src*	Name†	z‡	$\log(r_e)$§	m_B‖	M_B#	$\log(L_B/L_\odot)$**	$\log(L_X)$††	$\log(L_X/L_B)$‡‡	Type§§	Group‖‖
#1	NGC 547	0.018239	0.951	12.91	−21.42	10.73	42.25	31.52	E1	A 194
#8	NGC 541	0.018086	1.417	13.07	−21.25	10.66	40.83	30.17	S0	A 194
#23	NGC 543	0.017666	0.675	14.46	−19.80	10.09	39.08	28.99	S0	A 194
#27	[D80] 051	0.013219	0.730	14.45	−19.18	9.84	40.06	30.22	S0	A 194
#56	NGC 545	0.017806	1.704	12.97	−21.31	10.69	41.10	30.41	S0	A 194
#1	NGC 3312	0.009627	1.421	11.85	−21.10	10.60	40.94	30.34	Sb	A 1060
#3	NGC 3311	0.011985	1.979	12.08	−21.34	10.70	41.25	30.55	E2	A 1060
#5	NGC 3309	0.013593	1.337	12.12	−21.58	10.79	40.51	29.72	E3	A 1060
#11	[S96a] 028	0.039604	1.420	12.78	−23.24	11.46	41.28	29.82	SB	A 1060
#12	ESO501-G 047	0.016088	1.937	14.32	−19.74	10.06	40.42	30.36	S0	A 1060
#22	NGC 3308	0.011855	1.621	12.78	−20.62	10.41	40.22	29.81	S0	A 1060

* The names given in this survey.
† Galaxy names from NASA Extra-galactic Database (NED). The references for the names appearing in brackets are Stein 1996 [S96a] and Dressler 1984 [D80].
‡ Redshift values from NED.
§ Effective radius from RC3.
‖ The values for the blue apparent magnitude, m_B, by RC3.
Absolute blue magnitude, calculated from apparent magnitude and distance, as $M_B = m_B + 5 - 5\log(d)$.
** Blue-band luminosity in solar units, defined as $\log L_B = -0.4(M_B - 5.41)$.
†† X-ray luminosities ($< 4r_e$) of galaxies in $\mathrm{erg\,s^{-1}}$.
‡‡ Logarithmic X-ray to optical luminosity ratio.
§§ Morphological-type code from RC3.
‖‖ Name of the group to which the galaxy belongs.

Downloaded from https://academic.oup.com/pasj/article/58/6/931/1445864 by Yildiz Teknik University Library (YTU) user on 25 February 2022

blue magnitudes, M_B, were calculated using $M_B = m_B + 5 - 5\log(d)$, where d is the distance in parsecs. The blue-band luminosity values were determined using the relation $\log L_B = -0.4(M_B - 5.41)$. The X-ray counts were accumulated within $r_x = 45$ arcsec, which is the angular radius of 90% encircled energy for PN. X-ray emission can be considered to be compact, because $r_x \leq 4\,r_e$ for the majority of the sources. The dotted gray lines represent $\log(L_X/L_B) = 28$, 29, 30, and 31 for a visual aid. The straight line shows the average distribution of X-ray compact early-type galaxies and the dashed line is the relative 90% confidence limits reported by Matsushita (2001). There is a clear scatter in figure 7. The most striking feature is that the total L_X/L_B values of our sample are slightly higher than the compact early-type galaxies, e.g., $L_X/L_B = 6.0 \times 10^{29}\,\mathrm{erg\,s^{-1}}\,L_{B\odot}^{-1}$, for M 81 (Sarazin et al. 2001). This is due either to bright central AGNs or the contribution of more unresolved discrete sources than expected. NGC 547 (from A 194) is the most luminous X-ray source in our survey ($L_X = 10^{42.25}\,\mathrm{erg\,s^{-1}}$). The L_X/L_B relation of this elliptical galaxy resembles the X-ray extended elliptical NGC 5044 and cD galaxy NGC 4486 (of Virgo) from Matsushita 2001 (figure 7). The entire X-ray emission radius, r_x, is defined to be the distance from the X-ray peak to the radius where the emission level is $1\,\sigma$ higher than the surrounding background. Based on a radial profile investigation of our survey galaxies, we calculated an average radius of $r_x = 15''$. The X-ray radius of NGC 547 has the highest value of $r_x = 19.''8$, which can reasonably make the source an extended elliptical. NGC 547 is found to be much brighter than typical elliptical galaxies, as expected for normal cD galaxies (Sandage, Hardy 1973; Schombert 1986), and is located near the spatial and kinematical center of the host cluster, A 194. We could not find any study in the literature defining NGC 547 as a cD galaxy. There is a slight suspicion as to whether or not NGC 547 is the cD galaxy. On the other hand, one of the brightest lenticular (S0) galaxy NGC 541 from A 194 is reported to have an envelope by Jordán et al. (2004) based on the Hubble Space Telescope (HST) and Very Large Telescope (VLT) observations. These findings are considered as evidence that NGC 541 is the cD of A 194. From the L_X/L_B ratio, we do not notice any peculiarity for NGC 541 ($\log L_B, L_X = 10.66, 40.83$).

The X-ray to optical luminosity ratios of the central galaxies of A 1060 were also studied by Yamasaki et al. (2002) with Chandra. They report L_B/L_X ratios of 2.9×10^{30} and $1.3 \times 10^{30}\,\mathrm{erg\,s^{-1}}\,L_{B\odot}^{-1}$ for NGC 3311 and NGC 3309, respectively. The NGC 3311 L_B/L_X ratio from our study is 1.3-times higher than the Chandra result. However, NGC 3309 is a factor of 0.4 magnitude lower. Yamasaki et al. (2002) reports a possible underestimation of the luminosities by about a factor of 2 at the maximum as a result of the uncertainty of the quantum efficiency of the ACIS at the low-energy band. This can explain the result for NGC 3311. The luminosity differences could also be due to the different sizes of the integration regions. Other than that, the background integration region differs. We used an annulus of $60'' \leq R \leq 90''$ around the galaxies, whereas $R \leq 98''$ was used for analysis of the Chandra data. This may have introduced a slight difference in the ICM contribution to the source spectrum. Another possibility is the time variability of the non-negligible LLAGNs luminosity at the center of these galaxies (Chandra in 2001 June and XMM in 2004 June).

The S0 galaxy NGC 543 (#23 from A 194 field) has the lowest L_X/L_B value in our survey. It has $\log L_X/L_B = 28.99$, which is a factor of 5.5 less than the nearby bulge-dominated Sa galaxy NGC 1291 (Irwin et al. 2002). The X-ray to optical blue luminosity ratio of NGC 1291 is reported by Irwin et al. (2002) using Chandra as factor of 1.4 less than the elliptical galaxy NGC 4697 (Sarazin et al. 2001) and the S0 galaxy NGC 1553 (Blanton et al. 2001). This may be the result of not having luminous sources in NGC 543, as also stated for NGC 1291 by Irwin et al. (2002). NGC 543 either has a faint LLAGN or there is no central active nuclei. It probably has been striped of its X-ray emitting gas by a recent interaction with other galaxies or the ICM. The source [D80] 051 (#27 from A 194) is a foreground source and has the lowest blue-luminosity value, $L_B = 0.69 \times 10^{10}\,\mathrm{erg\,s^{-1}}\,L_{B\odot}^{-1}$. The source [S96a] 028 (#11) is a background SB from A 1060 field with $z = 0.0396$ (circled star in figure 7); therefore, we do not discuss this source along with the other cluster members.

The L_X/L_B plot (figure 7) was obtained for sources with optical counterparts, which was less than 10% of the X-ray sources. We show the L_X/L_B ratios for the other sources in the same figure. The limiting magnitude was set to $M_B = -18.64$ ($L_B = 10^{9.62}\,\mathrm{erg\,s^{-1}}\,L_{B\odot}^{-1}$) (private communication with H. Yamanoi). Considering the error ranges of the X-ray luminosity and the 90% confidence range of the average L_X/L_B distribution reported by Matsushita (2001), the X-ray emission from 13 more sources are found to be explained by unresolved LMXBs. To avoid any visual confusion, we indicate their locations with diamonds (figure 7), but do not present error bars. The remaining 52 sources, 68% of the X-ray sources, are not significantly contaminated by discrete sources. In other words, LMXBs are insufficient to explain the observed X-ray emission from these sources. They are either optically obscured or powered by some other physical mechanism so that they become bright in X-rays. The nature of X-Ray-bright optically normal galaxies (XBONGs) was well studied by Comastri et al. (2002) and Yuan et al. (2004). One explanation is that XBONGs are luminous AGNs, which is also an ideal solution for our result. We review the possibility of AGN-powered X-ray emission in the following section.

7.2. *X-Ray Luminosity Function*

If the X-ray excess emission is assumed to be produced by something other than discrete sources, e.g., active nuclei, the intrinsic XLF can be comparable to non-cluster fields. In this study, we compared our cluster results to two different fields: groups of galaxies and blank skies. Figure 8 shows the XLF computed for our survey. The gray crosses show the predicted XLF from the local group by Elvis et al. (1984). The diamonds show the luminosity function and the straight dashed line is the best-fit power-law of -2.75 by Piccinotti el al. (1982). As for the blank field, we employed the result of the cosmological evolution survey of Ueda et al. (2003), which is shown as the broken-dashed line. Ueda et al. studied AGNs brighter than $L_X = 10^{42}\,\mathrm{erg\,s^{-1}}$. In order to have the blank-field XLF for the lower luminosity levels of $L_X \leq 10^{42}\,\mathrm{erg\,s^{-1}}$, we extrapolated the XLF reported by Ueda et al. The extrapolation was estimated by an analytical expression of a smoothly connected

Downloaded from https://academic.oup.com/pasj/article/58/6/931/1445864 by Yildiz Teknik University Library (YTU) user on 25 February 2022

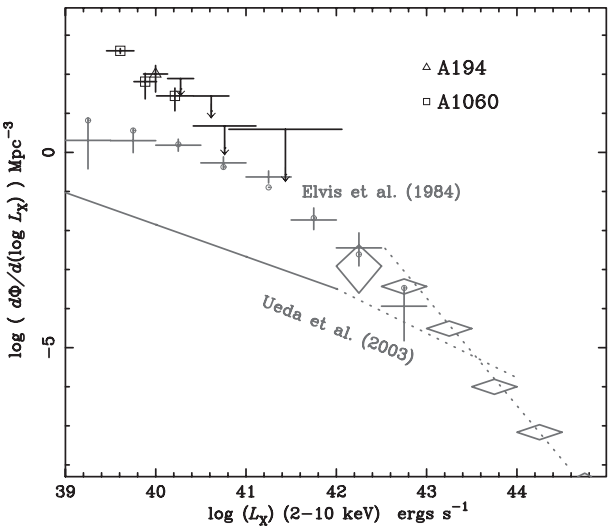


Fig. 8. Intrinsic X-ray luminosity function (XLF) of the sources in the 2–10 keV energy band. The black-crosses and solid-bars (stand for the upper-limits) are from cluster fields. The number density per unit volume per $\log L_{\rm X}$, $d\Phi(L_{\rm X})/d\log L_{\rm X}$, versus $L_{\rm X}$ is given in a logarithmically scaled plot. The gray crosses show the predicted XLF from local group by Elvis et al. (1984). The curved dashed line is the XLF for blank-fields, which is extrapolated from the result of Ueda et al. (2003) for the analytical formula [equation (4)] of Miyaji et al. (2000) (see subsection 7.2).

two power-law form, as defined by Miyaji et al. (2000),

$$\frac{d\Phi(L_{\rm X}, z=0)}{d\log L_{\rm X}} = A\left[\left(\frac{L_{\rm X}}{L_*}\right)^{\gamma 1} + \left(\frac{L_{\rm X}}{L_*}\right)^{\gamma 2}\right]^{-1}. \quad (4)$$

The $d\Phi(L_{\rm X}, z)/\log L_{\rm X}$ represents the volume density per $\log L_{\rm X}$ as a function of $L_{\rm X}$ and z. Using the best-fit parameters of the pure luminosity evolution (PLE) model from Ueda et al. (2003), ($A = 1.41 \times 10^{-6}\,{\rm Mpc}^{-3}$, $\log L_* = 43.66\,{\rm erg\,s^{-1}}$, $\gamma 1 = 0.82$, $\gamma 2 = 2.37$), we calculated the luminosity function for the local universe ($z \leq 0.02$). The black crosses at the top of figure 8 represent the computed XLF for the clusters. Our X-ray selected sources have luminosity values of $10^{39.6} \leq L_{\rm X} \leq 10^{41.4}\,{\rm erg\,s^{-1}}$. The luminosity restrictions are introduced by the instrumental incompleteness for faint sources and statistical shortage for bright sources. The source density gradually decreases for sources brighter than $L_{\rm X} \geq 10^{40.5}\,{\rm erg\,s^{-1}}$, at which point the source density is comparable to the field level. A source density excess is evident at low luminosity levels of $L_{\rm X} \leq 10^{40.5}\,{\rm erg\,s^{-1}}$. The source density for the clusters is found to be around 3 orders of magnitude higher than the field. Christlein and Zabludoff (2003) report a cluster source density as high as a factor 175 larger than the blank-fields in optical bands. An equal amount of overdensity in X-rays would be the expected level. There is a minimum of a factor of 6 higher source density observed in X-rays compared to the blank field. The excess is a factor of 15 higher relative to the source density of the local group, reported by Elvis et al. (1984). A comparison of the cluster source density with both non-cluster fields implies an elevated AGN activity in the cluster environment.

It is known that galaxies funnel toward clusters through filaments, where galaxies appear like pearls on a string. The projection effect may cause an enhancement of the source density, if a filament aligns through the line of sight. Simulations of the large scale formations (Governato et al. 1998) show a quantitatively higher number of densities on knots (clusters) than filaments. If one assumes that the observed X-ray excess is due to the projectional effects, the required length of a filament with a 1 Mpc average radius would be about 100 Mpc. Since the mean cluster separation is several 10 Mpc, the projection effect of the filamentary branches, itself, would be unrealistic. However, a partial enhancement from filaments is admitted.

Recent Chandra studies show that X-ray sources are not distributed randomly (Martini et al. 2002; Johnson et al. 2003). Bright sources are reported to populate at the outskirts, whereas faint ones are found somewhat nearer to the cluster center (< 1 Mpc). Based on the radial distribution of the sources, possibilities of AGN fueling and quenching are suggested by the Chandra results. Considering the restricted low luminosity range ($10^{39.6} \leq L_{\rm X} \leq 10^{41.4}\,{\rm erg\,s^{-1}}$) and X-ray to optical luminosity ratios ($L_{\rm X}/L_{\rm B}$) from our survey, the X-ray sources from the fields of A 194 and A 1060 are likely to be experiencing a similar physical situation. The fueling scenario can account for the excess for the faint sources, and the quenching can explain the population vanishing for the bright sources, as obtained from the XLF (figure 8). The dense cluster environments are the places with a high possibility of collisions and close encounters of galaxies in the vicinity of clusters. When a galaxy falls into the cluster gravitational potential, the balance between AGN and the surrounding gas is disturbed. The gas falls onto AGN and powers it. The infall induces AGN activity; therefore, the source becomes brighter. It is currently believed that most, if not all, galaxies, including our galaxy, host a Black Hole (BH) at its center. Most of them are inactive, and not accreting much matter. The physical conditions in the ICM may also awake these kinds of starved BHs, which increases the X-ray sources density in clusters. However, the mechanism reverses at smaller distances from the center as the galaxy loses a significant amount of its fuel by ram-pressure striping. The AGN activity is reduced by a deep cluster potential. In other words, the AGN activity decreases for longer residents. This explains why the source density vanishes at luminosity levels $L_{\rm X} \geq 10^{40.5}\,{\rm erg\,s^{-1}}$ and the absence of bright sources with $L_{\rm X} \geq 10^{42}\,{\rm erg\,s^{-1}}$ in nearby poor clusters.

8. Conclusions

We have presented the nature of X-ray detected sources in the fields of nearby, poor clusters of galaxies A 194 and A 1060. A total of 76 X-ray sources have been detected (46 and 32, respectively) by the PN camera. The X-ray spectra of several sources were studied for the first time, particularly the A 194 sources. Sources with low counting statistics were studied using the so-called X-ray color–diagrams. The best-fit values of the used plasma models are found to be in a reasonable range; the temperatures are sub keV levels ($kT \leq 1.0$ keV) and the photon indices are around $\Gamma = 1.7 \pm 1.0$. The excess of the X-ray sources at $F_{\rm X} = 1 \times 10^{-14}\,{\rm erg\,cm^{-2}\,s^{-1}}$ is estimated to be as $\sim 3\sigma$ from the $\log(N)$–$\log(S)$ plot. Considering the low

Downloaded from https://academic.oup.com/pasj/article/58/6/931/1445864 by Yildiz Teknik University Library (YTU) user on 25 February 2022

luminosity levels of our survey sample of $L_X \leq 10^{42}\,\mathrm{erg\,s^{-1}}$, the fractions of X-ray emission produced by LMXB, hot halo and LLAGN were evaluated separately. Based on the L_X/L_B relation, about 30% of the whole sample can be explained by X-ray emission from unresolved LMXBs. Since the spectroscopic redshift is available for 10% of the X-ray sources, the cluster source density is approximated by subtracting the field source density. The difference is attributed to galaxies in the cluster gravitational potential. The X-ray luminosity function exhibits a source density excess for the clusters by a factor of 6 higher than the blank field and a factor of 15 higher than the local group at $L_X \geq 10^{40.5}\,\mathrm{erg\,s^{-1}}$. The enhancement vanishes for the brighter sources. We suggest that AGN fueling is induced, and inactive BHs are awaken in the outskirts, whereas AGN activity is quenched in the cluster center.

We would like to thank Chiho Matsumoto and Yoshihiro Ueda for valuable discussions and Hitomi Yamanoi for providing the SUBARU observations of Abell 1060 before being published. This work is supported in part by a Grant-in-Aid for Scientific Research on Specially Promoted Research, contract No. 15001002, from the Ministry of Education, Sports, Culture, Science and Technology (MEXT), Japan. The author also acknowledges support for overseas research students by MEXT. This research made use of data obtained through the XMM-Newton, an ESA Science Mission with instruments and contributions directly funded by ESA Member states and the US (NASA).

Appendix. Source Counts and HR values

Table 6. For A 194.

Src.	Acronym R.A. Dec.	$R\sigma$ arcsec	Count rate (count ks^{-1}) SOFT	MID	HARD	HR1 (M − S)/(M + S)	HR2 (H − M)/(H + M)	$F_{[2-10]} \times 10^{-14}$ erg cm^{-2} s^{-1}	log L_X	Note	z_{opt}
(1)	(2)	(3)	(4)	(5)	(6)	(7)	(8)	(9)	(10)	(11)	(12)
1	XMMU J012600.5−012043	0.20	84.89 ± 3.30	19.70 ± 1.64	42.91 ± 2.39	−0.62 ± 0.03	0.37 ± 0.04	159.13	42.06	NGC 547	0.01823
2	XMMU J012535.9−012546	0.41	25.06 ± 1.64	10.80 ± 1.09	···	−0.40 ± 0.05	−1.00 ± 0.00	5.97	40.64		
3	XMMU J012549.3−012412	0.54	7.94 ± 0.95	3.72 ± 0.69	4.47 ± 0.77	−0.36 ± 0.10	0.09 ± 0.13	1.97	40.15		
4	XMMU J012602.8−012701	0.82	···	2.65 ± 0.59	9.28 ± 1.13	1.00 ± 0.00	0.56 ± 0.09	7.05	40.71		
5	XMMU J012529.6−011455	0.81	4.32 ± 0.92	5.33 ± 0.92	8.82 ± 1.54	0.10 ± 0.14	0.25 ± 0.12	6.61	40.68		
8	XMMU J012544.2−012247	0.51	35.35 ± 3.88	4.22 ± 1.16	8.67 ± 1.14	−0.79 ± 0.06	0.34 ± 0.13	3.62	40.42	NGC 541	0.01808
9	XMMU J012556.3−012515	0.57	10.62 ± 1.08	5.46 ± 0.76	3.10 ± 0.73	−0.32 ± 0.08	−0.28 ± 0.13	1.66	40.08		
10	XMMU J012611.0−012510	1.34	···	2.00 ± 0.55	···	1.00 ± 0.00	−1.00 ± 0.00	0.52	39.58		
11	XMMU J012540.1−011945	0.61	8.15 ± 1.03	3.72 ± 0.69	3.68 ± 0.76	−0.37 ± 0.10	−0.01 ± 0.14	1.41	40.01		
12	XMMU J012554.5−012343	0.57	10.46 ± 1.05	3.27 ± 0.62	···	−0.52 ± 0.08	−1.00 ± 0.00	1.97	40.16		
13	XMMU J012555.5−011119	1.00	6.10 ± 1.34	5.42 ± 1.17	···	−0.06 ± 0.15	−1.00 ± 0.00	4.04	40.47		
14	XMMU J012533.1−013333	1.73	4.53 ± 0.98	···	···	−1.00 ± 0.00	···	1.52	40.04		
16	XMMU J012541.3−012836	1.34	···	···	2.55 ± 0.62	···	1.00 ± 0.00	0.20	39.15		
17	XMMU J012554.5−012517	1.36	···	···	2.90 ± 0.69	−1.00 ± 0.00	1.00 ± 0.00	0.98	39.85		
18	XMMU J012538.7−013107	1.22	2.45 ± 0.65	···	3.50 ± 0.84	···	1.00 ± 0.00	0.40	39.46		
19	XMMU J012622.5−012654	1.34	···	···	6.66 ± 1.30	···	1.00 ± 0.00	2.75	40.30		
20	XMMU J012614.9−012240	1.44	···	···	3.49 ± 0.82	···	1.00 ± 0.00	0.75	39.73		
21	XMMU J012544.0−011728	0.70	7.11 ± 1.01	3.58 ± 0.67	3.19 ± 0.76	−0.33 ± 0.11	−0.06 ± 0.15	1.09	39.90		
22	XMMU J012635.5−012349	1.56	3.81 ± 0.98	2.65 ± 0.76	···	−0.18 ± 0.19	−1.00 ± 0.00	0.53	39.58		
24	XMMU J012551.7−012919	0.97	5.78 ± 0.92	2.84 ± 0.60	2.54 ± 0.63	−0.34 ± 0.12	−0.06 ± 0.16	1.25	39.96		
25	XMMU J012612.0−012904	0.94	4.79 ± 0.88	2.68 ± 0.61	5.17 ± 1.09	−0.28 ± 0.13	0.32 ± 0.14	1.87	40.13		
28	XMMU J012556.5−012732	0.92	4.54 ± 0.78	···	···	−1.00 ± 0.00	···	0.13	38.97		
29	XMMU J012503.2−012244	0.81	8.32 ± 1.32	5.20 ± 0.97	10.20 ± 1.68	−0.23 ± 0.12	0.32 ± 0.11	6.36	40.66		
30	XMMU J012611.2−012802	1.42	3.48 ± 0.75	···	···	−1.00 ± 0.00	···	1.19	39.94		
31	XMMU J012531.9−012232	0.95	4.19 ± 0.76	2.44 ± 0.59	···	−0.26 ± 0.14	−1.00 ± 0.00	1.42	40.01		
32	XMMU J012539.3−011309	1.05	6.86 ± 1.51	···	6.73 ± 1.83	−1.00 ± 0.00	1.00 ± 0.00	5.11	40.57		
33	XMMU J012539.1−012126	0.90	4.13 ± 0.78	2.26 ± 0.54	2.79 ± 0.67	−0.29 ± 0.14	0.10 ± 0.17	1.06	39.88		
35	XMMU J012600.5−012747	1.19	3.12 ± 0.71	···	2.74 ± 0.69	−1.00 ± 0.00	1.00 ± 0.00	2.18	40.20		
36	XMMU J012612.2−012953	2.16	6.15 ± 1.64	···	···	−1.00 ± 0.00	···	11.87	40.93		
37	XMMU J012557.9−011717	0.89	7.95 ± 1.13	3.21 ± 0.67	3.91 ± 0.87	−0.43 ± 0.10	0.10 ± 0.15	0.88	39.81		
38	XMMU J012611.1−011155	0.61	28.23 ± 2.69	10.10 ± 1.59	6.44 ± 1.71	−0.47 ± 0.07	−0.22 ± 0.15	0.70	39.71		
41	XMMU J012610.6−012349	1.59	···	···	4.42 ± 0.89	···	1.00 ± 0.00	2.42	40.24		
43	XMMU J012510.7−011542	0.93	13.65 ± 1.74	5.58 ± 1.27	···	−0.42 ± 0.11	−1.00 ± 0.00	2.85	40.32		
44	XMMU J012624.6−012415	1.76	2.76 ± 0.72	···	···	−1.00 ± 0.00	···	0.81	39.77		
45	XMMU J012513.0−012802	1.27	3.33 ± 0.78	2.18 ± 0.64	5.06 ± 1.12	−0.21 ± 0.18	0.40 ± 0.15	1.01	39.87	RadioS.	
46	XMMU J012556.6−012610	2.62	···	···	2.97 ± 0.70	···	1.00 ± 0.00	8.92	40.81		
47	XMMU J012554.9−012927	1.46	2.73 ± 0.68	2.17 ± 0.53	3.05 ± 0.79	−0.11 ± 0.17	0.17 ± 0.17	5.10	40.57		
48	XMMU J012508.2−011815	1.81	···	2.81 ± 0.80	···	1.00 ± 0.00	−1.00 ± 0.00	0.54	39.59		
49	XMMU J012528.6−012430	1.93	4.47 ± 0.94	···	···	−1.00 ± 0.00	···	0.02	38.04		
50	XMMU J012534.3−011640	5.23	3.40 ± 0.84	···	···	−1.00 ± 0.00	···	1.61	40.07		
51	XMMU J012601.9−012808	3.26	2.32 ± 0.60	···	···	−1.00 ± 0.00	···	4.33	40.50		
52	XMMU J012606.1−011744	3.41	3.41 ± 0.83	···	···	−1.00 ± 0.00	···	0.35	39.40		
53	XMMU J012627.9−011808	3.92	4.15 ± 1.23	···	···	−1.00 ± 0.00	···	0.28	39.31		
54	XMMU J012544.0−012732	2.04	2.97 ± 0.70	···	···	−1.00 ± 0.00	···	···	···		
55	XMMU J012623.7−011733	2.42	5.15 ± 1.29	···	···	−1.00 ± 0.00	···	0.65	39.67		
56	XMMU J012559.0−012027	···	26.72 ± 1.84	11.29 ± 1.22	10.19 ± 1.33	−0.05 ± 0.08	−0.41 ± 0.12	10.77	40.89	NGC 545	0.01780

(1) Source number in this survey. (2) Acronym with R.A.-Dec. (3) Positional errors in arcsec. (4), (5), (6) The source counts in ks for soft, medium and hard band. (7) Hardness ratio 1, HR1 = (M − S)/(M + S). (8) Hardness ratio 2, HR2 = (H − M)/(H + M). (9) Flux in 2–10 keV. (10) Luminosity in 2–10 keV. (11) Counterpart in other bands. (12) optical redshift.

Downloaded from https://academic.oup.com/pasj/article/58/6/931/1445864 by Yildiz Teknik University Library (YTU) user on 25 February 2022

Table 7. For A 1060.

Src.	Acronym R.A. Dec.	$R\sigma$	Count rate (count ks^{-1})			HR1	HR2	$F_{[2-10]} \times 10^{-14}$	log L_X	Note	z_{opt}
		arcsec	SOFT	MEDIUM	HARD	(M − S)/(M + S)	(H − M)/(H + M)	erg cm^{-2} s^{-1}	erg s^{-1}		
(1)	(2)	(3)	(4)	(5)	(6)	(7)	(8)	(9)	(10)	(11)	(12)
1	XMMU J103702.7−273354.5	0.22	23.23 ± 1.42	6.60 ± 0.83	39.74 ± 1.83	−0.56 ± 0.05	0.72 ± 0.03	51.05	41.12	NGC 3312	0.00962
2	XMMU J103616.2−273945.4	0.44	···	4.01 ± 0.84	23.03 ± 1.79	1.00 ± 0.00	0.70 ± 0.06	10.32	40.42		
3	XMMU J103643.0−273142.8	0.27	40.40 ± 1.78	23.04 ± 1.38	18.08 ± 1.44	−0.27 ± 0.03	−0.12 ± 0.05	23.35	40.78	NGC 3311	0.01198
4	XMMU J103626.9−273819.6	0.32	24.56 ± 1.54	9.59 ± 1.03	13.78 ± 1.31	−0.44 ± 0.05	0.18 ± 0.07	5.98	40.18		
5	XMMU J103635.9−273106.9	0.27	41.19 ± 1.84	16.59 ± 1.28	8.01 ± 1.14	−0.43 ± 0.04	−0.35 ± 0.07	1.39	39.55	NGC 3309	0.01359
6	XMMU J103715.0−272532.5	0.36	21.57 ± 1.43	7.84 ± 0.91	9.04 ± 1.12	−0.47 ± 0.05	0.07 ± 0.08	2.16	39.74		
7	XMMU J103625.9−273729.5	0.38	15.04 ± 1.29	6.35 ± 0.88	11.97 ± 1.24	−0.41 ± 0.07	0.31 ± 0.08	4.51	40.06		
8	XMMU J103645.6−272559.2	0.46	8.36 ± 0.96	5.44 ± 0.76	6.67 ± 0.89	−0.21 ± 0.09	0.10 ± 0.10	2.05	39.72		
9	XMMU J103658.4−272057.1	0.57	10.14 ± 1.17	5.87 ± 0.85	5.93 ± 1.10	−0.27 ± 0.09	0.01 ± 0.12	2.88	39.87		
10	XMMU J103659.8−273028.6	0.41	13.04 ± 1.08	6.86 ± 0.82	6.20 ± 0.88	−0.31 ± 0.07	−0.05 ± 0.09	3.03	39.89		
11	XMMU J103628.6−272237.2	0.48	9.64 ± 1.11	4.46 ± 0.78	11.07 ± 1.25	−0.37 ± 0.09	0.43 ± 0.09	3.59	39.96	[S96a] 028	0.03960
12	XMMU J103717.2−272809.1	0.78	4.20 ± 0.79	2.39 ± 0.59	6.60 ± 0.94	−0.27 ± 0.14	0.47 ± 0.11	4.04	40.01	ESO501-G47	0.01608
13	XMMU J103714.2−273306.6	0.84	3.93 ± 0.84	4.05 ± 0.87	4.79 ± 0.96	0.02 ± 0.15	0.08 ± 0.15	2.71	39.84		
14	XMMU J103638.7−274250.7	0.89	···	4.41 ± 0.81	7.59 ± 1.24	1.00 ± 0.00	0.26 ± 0.11	4.77	40.09		
15	XMMU J103643.3−271927.5	1.32	···	···	5.42 ± 1.19	···	1.00 ± 0.00	3.81	39.99		
16	XMMU J103712.8−274102.8	1.21	8.22 ± 1.10	···	···	−1.00 ± 0.00	···	4.63	40.07	NGC 3314	∗
17	XMMU J103610.4−272850.4	1.13	5.35 ± 0.93	···	3.84 ± 0.93	−1.00 ± 0.00	1.00 ± 0.00	1.25	39.50		
18	XMMU J103620.0−273927.3	1.14	6.94 ± 1.13	···	···	−1.00 ± 0.00	···	···	···		
19	XMMU J103729.1−274234.7	1.34	···	4.73 ± 0.95	···	1.00 ± 0.00	−1.00 ± 0.00	4.36	40.05		
20	XMMU J103638.6−271843.8	0.98	5.50 ± 1.01	···	6.04 ± 1.25	−1.00 ± 0.00	1.00 ± 0.00	0.18	38.66		
21	XMMU J103748.7−272959.7	1.10	10.48 ± 1.33	3.14 ± 0.79	···	−0.54 ± 0.10	−1.00 ± 0.00	2.27	39.76		
22	XMMU J103622.5−272618.9	0.77	7.97 ± 1.04	···	···	−1.00 ± 0.00	···	0.13	38.5	NGC 3308	0.01185
23	XMMU J103629.9−272133.4	1.05	3.35 ± 0.80	2.62 ± 0.70	···	−0.12 ± 0.18	−1.00 ± 0.00	0.12	38.48		
24	XMMU J103603.5−272958.6	1.06	5.58 ± 0.98	···	···	−1.00 ± 0.00	···	1.72	39.64		
25	XMMU J103704.4−272358.1	1.39	3.37 ± 0.90	···	···	−1.00 ± 0.00	···	1.48	39.58	[S96a] 057	0.00916
26	XMMU J103709.3−273513.2	0.82	6.31 ± 0.83	2.75 ± 0.60	···	−0.39 ± 0.11	−1.00 ± 0.00	1.73	39.65		
27	XMMU J103558.0−273002.4	1.52	4.53 ± 0.92	···	···	−1.00 ± 0.00	···	0.90	39.36		
28	XMMU J103737.1−273601.5	1.74	5.21 ± 1.29	···	16.29 ± 3.86	−1.00 ± 0.00	1.00 ± 0.00	2.64	39.83		
29	XMMU J103650.7−273549.6	1.27	3.51 ± 0.81	3.71 ± 0.72	3.71 ± 0.82	0.03 ± 0.15	0.00 ± 0.15	0.68	39.24		
30	XMMU J103645.4−274157.2	1.01	7.62 ± 1.02	···	3.73 ± 0.94	−1.00 ± 0.00	1.00 ± 0.00	1.31	39.46		
31	XMMU J103737.5−272900.8	2.37	···	2.41 ± 0.65	···	1.00 ± 0.00	−1.00 ± 0.00	4.52	40.06		
32	XMMU J103634.8−274159.8	1.42	3.75 ± 0.86	2.69 ± 0.71	···	−0.16 ± 0.17	−1.00 ± 0.00	3.67	39.97		

∗: NGC 3314 is a galaxy pair, having z = 00951 (NGC 3314A) and z = 01548 (NGC 3314B).
(1) Source number in this survey. (2) Acronym with R.A.-Dec. (3) Positional errors in arcsec. (4), (5), (6) The source counts in ks for soft, medium and hard band. (7) Hardness ratio 1, HR1 = (M − S)/(M + S). (8) Hardness ratio 2, HR2 = (H − M)/(H + M). (9) Flux in 2–10 keV. (10) Luminosity in 2–10 keV. (11) Counterpart in other bands. (12) optical redshift.

References

Blanton, E. L., Sarazin, C. L., & Irwin, J. A. 2001, ApJ, 552, 106
Cappelluti, N., Cappi, M., Dadina, M., Mazzotta, P., Elvis, M., Malaguti, G., Branchesi, M., D'Elia, V., & Palumbo, G. G. C. 2005, A&A, 430, 39
Cappi, M., et al. 2001, ApJ, 548, 624
Cash, W. 1979, ApJ, 228, 939
Christlein, D., & Zabludoff, A. I. 2003, ApJ, 591, 764
Comastra, A., et al. 2002, astro-ph/0203019
Damiani, F., Maggio, A., Micela, G., & Sciortino, S. 1997, ApJ, 483, 350
de Vaucouleurs, G., de Vaucouleurs, A., Corwin, H. G., Jr., Buta, R. J., Paturel, G., & Fouque, P. 1991, Third Reference Catalogue of Bright Galaxies (RC3 Catalog) (New York: Springer-Verlag)
Dressler, A. 1980, ApJS, 42, 565
Dressler, A., Gunn, J. E., & Schneider, D. P. 1985, ApJ, 294, 70
Dressler, A., Smail, I., Poggianti, B. M., Butcher, H., Couch, W. J., Ellis, R. S., & Oemler, A., Jr. 1999, ApJS, 122, 51
Elvis, M., Soltan, A., & Keel, W. C. 1984, ApJ, 283, 479
Finoguenov, A., Briel, U. G., Henry, J. P., Gavazzi, G., Iglesias-Paramo, J., & Boselli, A. 2004, A&A, 419, 47
Georgantopoulos, I., Georgakakis, A., & Koulouridis, E. 2005, MNRAS, 360, 782
Gisler, G. R. 1978, MNRAS, 183, 633
Governato, F., Baugh, C. M., Frenk, C. S., Cole, S., Lacey, C. G., Quinn, T., & Stadel, J. 1998, Nature, 392, 359
Hasinger, G., et al. 2001, A&A, 365, L45
Henry, J. P., & Briel, U. G. 1991, A&A, 246, L14
Irwin, J. A., Sarazin, C. L., & Bregman, J. N. 2002, ApJ, 570, 152
Johnson, O., Best, P. N., & Almaini, O. 2003, MNRAS, 343, 924
Jordán, A., Côté, P., West, M. J., Marzke, R. O., Minniti, D., & Rejkuba, M. 2004, AJ, 127, 24
Kahabka, P., & van den Heuvel, E. P. J. 1997, ARA&A, 35, 69
Kirsch, M. 2006, XMM-Newton Science Ops. Centre Technical Note, XMM-SOC-CAL-TN-0018
Lazzati, D., Campana, S., Rosati, P., Chincarini, G., & Giacconi, R. 1998, A&A, 331,41
Mainieri, V., Bergeron, J., Hasinger, G., Lehmann, I., Rosati, P., Schmidt, M., Szokoly, G., & Della Ceca, R. 2002, A&A, 393, 425
Martini, P., Kelson, D. D., Kim, E., Mulchaey, J. S., & Athey, A. A. 2006, 644, 116
Martini, P., Kelson, D. D., Mulchaey, J., & Trager, S. C. 2002, ApJ, 576, L109
Matsushita, K. 2001, ApJ, 547, 693
Mewe, R., Gronenschild, E. H. B. M., & van den Oord, G. H. J. 1985, A&AS, 62, 197
Miyaji, T., Hasinger, G., & Schmidt, M. 2000, A&A, 353, 25

Downloaded from https://academic.oup.com/pasj/article/58/6/931/1445864 by Yildiz Teknik University Library (YTU) user on 25 February 2022

Molnar, S. M., Hughes, J. P., Donahue, M., & Joy, M. 2002, ApJ, 573, L91
Oemler, A., Jr. 1974, ApJ, 194, 1
Osterbrock, D. E. 1960, ApJ, 132, 325
Page, M. J., & Carrera, F. J. 2000, MNRAS, 311, 433
Piccinotti, G., Mushotzky, R. F., Boldt, E. A., Holt, S. S., Marshall, F. E., Serlemitsos, P. J., & Shafer, R. A. 1982, ApJ, 253, 485
Pietsch, W., Freyberg, M., & Haberl, F. 2005, A&A, 434, 483
Ruderman, J. T., & Ebeling, H. 2005, ApJ, 623, 81
Sandage, A., & Hardy, E. 1973, ApJ, 183, 743
Sarazin, C. L., Irwin, J. A., & Bregman, J. N. 2001, ApJ, 556, 533
Saxton, R. D. 2003, XMM-Newton Science Ops. Centre Technical Note, XMM-SOC-CAL-TN-0023
Schombert, J. M. 1986, ApJS, 60, 603
Soltan, A., Freyberg, M. J., & Trümper, J. 2001, A&A, 378, 735
Stein, P. 1996, A&AS, 116, 203
Strüder, L., et al. 2001, A&A, 365, L18
Sun, M., & Murray, S. S. 2002, ApJ, 577, 139
Turner, M. J. L., et al. 2001, A&A, 365, L27
Ueda, Y., Akiyama, M., Ohta, K., & Miyaji, T. 2003, ApJ, 598, 886
White, N. E., & Marshall, F. E. 1984, ApJ, 281, 354
Yamasaki, N. Y., Ohashi, T., & Furusho, T. 2002, ApJ, 578, 833
Yuan, F., & Narayan, R. 2004, ApJ, 612, 724

Downloaded from https://academic.oup.com/pasj/article/58/6/931/1445864 by Yildiz Teknik University Library (YTU) user on 25 February 2022